

Cross-talk free and ultra-compact fiber optic sensor for simultaneous measurement of temperature and refractive index

Hae Young Choi, Gopinath Mudhana, Kwan Seob Park, Un-Chul Paek, and Byeong Ha Lee*

*Department of Information and Communications, Gwangju Institute of Science and Technology,
1 Oryong-dong, Buk-Gu, Gwangju, 500-712, South Korea*

**leebh@gist.ac.kr*

Abstract: We propose and demonstrate a cross-talk free simultaneous measurement system for temperature and external refractive index (ERI) implemented by dual-cavity Fabry-Perot (FP) fiber interferometer. The sensing probe consists of two cascaded FP cavities formed with a short piece of multimode fiber (MMF) and a micro-air-gap made of hollow core fiber (HOF). The fabricated sensor head was ultra-compact; the total length of the sensing part was less than 600 μm . Since the reflection spectrum of the composite FP structures is given by the superposition of each cavity spectrum, the spectrum measured in the wavelength domain was analyzed in the Fourier or spatial frequency domain. The experimental results showed that temperature could be determined independently from the spatial frequency shift without being affected by the ERI, while the ERI could be also measured solely by monitoring the intensity variation in the spatial frequency spectrum. The ERI and the temperature sensitivities were approximately 16 dB/RIU for the 1.33-1.45 index range, and 8.9 nm/ $^{\circ}\text{C}$ at low temperature and 14.6 nm/ $^{\circ}\text{C}$ at high temperature, respectively. In addition, it is also demonstrated that the proposed dual-cavity FP sensor has potential for compensating any power fluctuation that might happen in the input light source.

©2009 Optical Society of America

OCIS codes: (060.2340) Fiber optic components; (060.2370) Fiber optic sensors.

References and links

1. B. Culshaw, "Optical Fiber Sensor Technologies: Opportunities and - Perhaps - Pitfalls," *J. Lightwave Technol.* **22**(1), 39–50 (2004).
2. Y. J. Rao, "Recent progress in applications of in-fibre Bragg grating sensors," *Opt. Lasers Eng.* **31**(4), 297–324 (1999).
3. S. W. James, and R. P. Tatam, "Optical fibre long-period grating sensors: characteristics and application," *Meas. Sci. Technol.* **14**(5), R49–R61 (2003).
4. Y. Jung, S. Kim, D. Lee, and K. Oh, "Compact three segmented multimode fibre modal interferometer for high sensitivity refractive-index measurement," *Meas. Sci. Technol.* **17**(5), 1129–1133 (2006).
5. O. Frazão, J. M. Baptista, and J. L. Santos, "Recent advances in high-birefringence fiber loop mirror sensors," *Sensors* **7**(11), 2970–2983 (2007).
6. M. J. Kim, Y. H. Kim, G. Mudhana, and B. H. Lee, "Simultaneous Measurement of Temperature and Strain Based on Double Cladding Fiber Interferometer Assisted by Fiber Grating Pair," *IEEE Photon. Technol. Lett.* **20**(15), 1290–1292 (2008).
7. T. Guo, X. Qiao, Z. Jia, Q. Zhao, and X. Dong, "Simultaneous measurement of temperature and pressure by a single fiber Bragg grating with a broadened reflection spectrum," *Appl. Opt.* **45**(13), 2935–2939 (2006).
8. P. Lu, L. Men, K. Sooley, and Q. Chen, "Tapered fiber Mach-Zehnder interferometer for simultaneous measurement of refractive index and temperature," *Appl. Phys. Lett.* **94**(13), 131110 (2009).
9. T. Zhu, Y.-J. Rao, and Q.-J. Mo, "Simultaneous measurement of Refractive Index and Temperature using a single ultralong-Period fiber grating," *IEEE Photon. Technol. Lett.* **17**(12), 2700–2702 (2005).
10. X. Shu, B. A. L. Gwandu, Y. Liu, L. Zhang, and I. Bennion, "Sampled fiber Bragg grating for simultaneous refractive-index and temperature measurement," *Opt. Lett.* **26**(11), 774–776 (2001).

11. A. Iadicco, S. Campopiano, A. Cutolo, M. Giordano, and A. Cusano, "Nonuniform thinned fiber Bragg gratings for simultaneous refractive index and temperature measurements," *IEEE Photon. Technol. Lett.* **17**(7), 1495–1497 (2005).
12. H. Y. Choi, K. S. Park, and B. H. Lee, "Photonic crystal fiber interferometer composed of a long period fiber grating and one point collapsing of air holes," *Opt. Lett.* **33**(8), 812–814 (2008).
13. Z. Tian, S. S.-H. Yam, J. Barnes, W. Bock, P. Greig, J. M. Fraser, H.-P. Loock, and R. D. Oleschuk, "Refractive index sensing with Mach-Zehnder interferometer based on concatenating two single-mode fiber tapers," *IEEE Photon. Technol. Lett.* **20**(8), 626–628 (2008).
14. X. Wan, and H. F. Taylor, "Intrinsic fiber Fabry-Perot temperature sensor with fiber Bragg grating mirrors," *Opt. Lett.* **27**(16), 1388–1390 (2002).
15. T. Wei, Y. Han, H.-L. Tsai, and H. Xiao, "Miniaturized fiber inline Fabry-Perot interferometer fabricated with a femtosecond laser," *Opt. Lett.* **33**(6), 536–538 (2008).
16. D. W. Kim, Y. Zhang, K. L. Cooper, and A. Wang, "In-fiber reflection mode interferometer based on a long-period grating for external refractive-index measurement," *Appl. Opt.* **44**(26), 5368–5373 (2005).
17. L.-Yuana, L.-Zhou, and J. Wu, "Fiber optic temperature sensor with duplex Michelson interferometric technique," *Sens. Actuators A Phys.* **86**(1-2), 2–7 (2000).
18. J. S. Sirkis, D. D. Brennan, M. A. Putman, T. A. Berkoff, A. D. Kersey, and E. J. Friebele, "In-line fiber étalon for strain measurement," *Opt. Lett.* **18**(22), 1973–1975 (1993).
19. X. Wan, H. F. Taylor, K. L. Cooper, and A. Wang, "Intrinsic fiber Fabry-Perot temperature sensor with fiber Bragg grating mirrors," *Opt. Lett.* **27**(16), 1388–1390 (2002).
20. H. Y. Choi, K. S. Park, S. J. Park, U.-C. Paek, B. H. Lee, and E. S. Choi, "Miniature fiber-optic high temperature sensor based on a hybrid structured Fabry-Perot interferometer," *Opt. Lett.* **33**(21), 2455–2457 (2008).
21. Y.-J. Rao, "Recent progress in fiber-optic extrinsic Fabry-Perot interferometric sensors," *Opt. Fiber Technol.* **12**(3), 227–237 (2006).
22. D. W. Kim, F. Shen, X. Chen, and A. Wang, "Simultaneous measurement of refractive index and temperature based on a reflection-mode long-period grating and an intrinsic Fabry-Perot interferometer sensor," *Opt. Lett.* **30**(22), 3000–3002 (2005).
23. Y. Zhang, X. C. Y. Wang, K. L. Cooper, and A. Wang, "Microgap Multicavity Fabry-Pérot Biosensor," *J. Lightwave Technol.* **25**, 1797–1804 (2007).
24. Y.-J. Rao, M. Deng, T. Zhu, and H. Li, "In-Line Fabry-Pérot Etalons Based on Hollow-Core Photonic Bandgap Fibers for High-Temperature Applications," *J. Lightwave Technol.* **27**(19), 4360–4365 (2009).
25. W.-H. Tsai, and C.-J. Lin, "A Novel Structure for the Intrinsic Fabry-Perot Fiber-Optic Temperature Sensor," *J. Lightwave Technol.* **19**(5), 682–686 (2001).
26. Z. L. Ran, Y. J. Rao, W. J. Liu, X. Liao, and K. S. Chiang, "Laser-micromachined Fabry-Perot optical fiber tip sensor for high-resolution temperature-independent measurement of refractive index," *Opt. Express* **16**(3), 2252–2263 (2008).
27. H. Y. Choi, M. J. Kim, and B. H. Lee, "All-fiber Mach-Zehnder type interferometers formed in photonic crystal fiber," *Opt. Express* **15**(9), 5711–5720 (2007).

1. Introduction

Varieties of fiber-based sensors have been proposed and developed for the measurements of physical, chemical and biological parameters [1–4]. Compared with traditional electric sensors, fiber optic sensors offer lots of advantages including electromagnetic interference immunity, multiplexing capability of several sensors in series, and resistance to harsh environment such as high temperature and big pressure. In particular, fiber optic sensors have received much attention recently because they can offer the advanced sensing ability which is able to simultaneously measure multi-parameters including strain, pressure, temperature and external refractive index (ERI) [5–8]. Simultaneous monitoring of temperature and ERI is one of the most important issues for applications in chemical, environmental and biomedical industries.

Sensors based on fiber Bragg gratings (FBGs) and long period fiber gratings (LPGs) have been typically used for temperature and ERI measurement [9–11]. However, grating-based sensors have inherently cross-sensitivity problem and also require expensive fabrication equipments, which restrict their practical applications. The interferometer techniques using the configurations of Mach-Zehnder [12,13], Fabry-Perot (FP) [14,15] and Michelson [16,17] are also well-known approaches to implement the fiber-optic sensors. However, they have also some drawbacks that need to be overcome. For example, some interferometer sensors are fragile, unstable, or not cost-effective. Nevertheless, sensors based on all-fiber interferometer are definitely the most attractive ones owing to high sensitivity and un-limited measuring wavelength range. Among them, the FP interferometer sensors are particularly attractive owing to simple configuration, small cross sensitivity and miniature sensor head [18–21].

Most recently, hybrid-structured FP interferometric sensors have been introduced and used for simultaneous temperature and ERI measurement [22,23]. Even though, the reported schemes were suitable for simultaneous measurement and could improve the sensitivity, they needed expensive and complicated fabrication processes due to the reflection-mode LPG [22] and the chemical etching process [23]. An air-cavity temperature sensor was reported by splicing a hollow-core photonic crystal between two SMF fibers [24]. Although it overcomes complicated fabrication processes by using splicing, it still requires relatively expensive photonic crystal fiber. Further, it measures the temperature and not ERI.

In this paper, we report an ultra-compact, cross-talk free sensor suitable for simultaneous temperature and ERI measurements. A short piece of multimode fiber (MMF) is fusion spliced to a conventional single mode fiber (SMF) with a tiny air gap made by inserting a small piece of hollow core fiber (HOF) between them. The air gap and the MMF form independent FP cavities. The air gap cavity is affected only by temperature, in this scheme, while the MMF cavity is affected by temperature and the ERI at its end face, so that the two measurands can be separated without cross-talk at least in principle. With the reflection spectrum of the proposed hybrid FP sensor, by taking the fast Fourier transformation (FFT), we could separate them successfully. One further advantage of this technique is that the unwanted power fluctuation of the light source can be compensated with the signal originated from the air gap cavity. It is also notable that only simple and cost effective fabrication processes are used.

2. Fabrication of dual-cavity Fabry-Perot interferometer

The fabrication of sensor tip or head was performed with a commercial fusion splicer (S183PM, FITEC Co.) and an in-house designed fiber cleaving system, shown in Fig. 1. The cleaving system consists of three parts; left and right fiber-holding assemblies and a fiber cleaver positioned between them. The left fiber holding assembly is composed of a fixed fiber holder and a movable (sliding) holder, while the right fiber holding assembly is composed of only one fixed fiber holder. The movable holder aids in removing the fiber from the cleaving assembly for splicing, while the fixed holder helps in marking the initial position of the fiber. The fiber cleaver in the middle is mounted on a 3-axis translation stage with a digital read-out of the x-axis movement for accurately adjusting the desired length of the fiber.

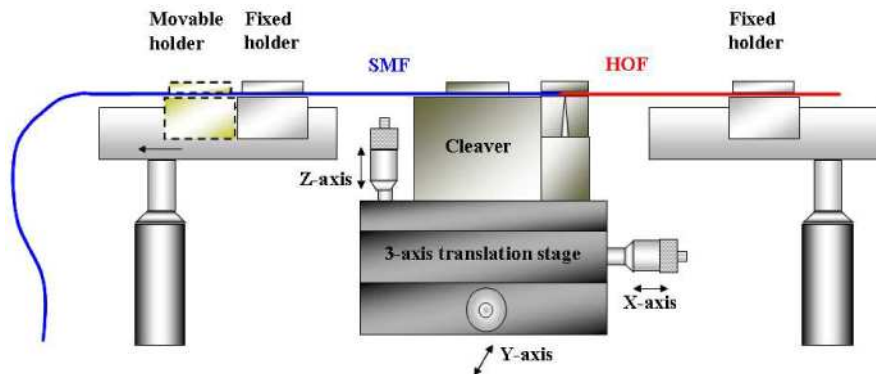


Fig. 1. Schematic of the cleaving system specially designed for the proposed sensor. It consists of three parts; two fixed fiber holders and a fiber cleaver that is mounted on a 3-axis translation stage. For the fiber splicing a movable holder, in addition to the fixed holder, is introduced at the left assembly. SMF: Single mode fiber. HOF: hollow optical fiber.

First, a piece of conventional SMF, which is held by the movable fiber holder, was placed in the cleaving system and cleaved. After the cleaving, the SMF was removed from the cleaving system together with the movable holder for the fusion splicing with a piece of HOF. After the splicing, the movable fiber holder along with the SMF-HOF piece was placed back in the same position of the cleaving system. The fixed fiber holder on the left fiber holding

assembly helps the movable fiber holder to find its original position. Then, the cleaver was precisely translated by the translation stage in order to get the desired length of HOF. The SMF-HOF structure was cleaved and spliced with a MMF to form the final composite. Finally, the other end of the MMF was cleaved at a certain length also, which forms the final sensing probe. With the in-house fabricated cleaving system described above, we could acquire the cleaving length with an error less than $\pm 5 \mu\text{m}$.

During the fabrication process, the reflection power and/or the spectrum were monitored with an optical spectrum analyzer (OSA) (Agilent, 86142B) to check the quality of the fiber cleaving and the contrast of the interference fringe. The reflectivity at the fiber-and-air interface can be calculated simply using the well-known Fresnel formula [25]

$$R = \left| \frac{n_0 - n_1}{n_0 + n_1} \right|^2 \quad (1)$$

where, n_0 and n_1 are the refractive indices of air and the fiber core, respectively. The measured reflectivity with the SMF and the MMF were about 3.4% and 3.7%, respectively. Owing to the appreciable reflectivity at the fiber-and-air interface, by locating a short piece of HOF between the SMF and the MMF piece as shown with Fig. 2, we could form two FP cavities in series; the air gap cavity composed only with the HOF and the fiber piece cavity composed with only MMF piece.

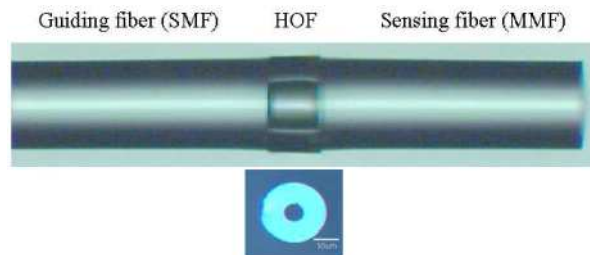


Fig. 2. Microscope image of the fabricated FP sensor. The HOF cavity and the MMF cavity lengths were designed to be $70 \mu\text{m}$ and $500 \mu\text{m}$, respectively. The inset is the cross-section image of HOF.

However, since HOF is not a well-defined optical waveguide, it causes additional transmission loss in the system. Therefore, the length of HOF piece must be optimized to obtain interference fringes with high contrast. To get the optimization, we have fabricated several cavities with different lengths of HOF, and experimentally measured the reflection spectra as shown in Fig. 3. With the HOF length of $50 \mu\text{m}$, as shown with Fig. 3(a), we had the reflection spectrum of Fig. 3(b). It had a good fringe contrast but sparse fringe appearance (about 8 fringes over 200 nm span). However, with the $150 \mu\text{m}$ long air-cavity, Fig. 3(e), we could have a dense fringe appearance (about 24 fringes over 200 nm span) but the contrast became poor, as shown with Fig. 3(f). With the moderate air-cavity length of about $100 \mu\text{m}$, as shown with Fig. 3(c) and (d), we had a good fringe contrast and also moderate fringe appearance (about 16 fringes over 200 nm span). Therefore, we have considered $50\text{-}100 \mu\text{m}$ as the optimum HOF length and maintained in the experiment. A too much long HOF length gave a much poor interference fringe contrast. It was due to the large insertion loss of the long HOF or air-cavity. It is noted that HOF is not a well-defined waveguide; at the core of it, a beam propagates with an appreciable divergence angle.

In addition to the air-cavity length, the splicing conditions of the HOF also affected the performance, especially the interference fringe contrast. When a high arc power or/and long arc duration time were employed for SMF-HOF splicing, the reflectivity was found to reduce drastically due to the hollow-core collapsing of the HOF and give poor fringe contrast. After several trials, the optimum arc-power and arc-time were found to be 100 units and 400 ms,

respectively. Optimum splicing conditions for HOF-MMF case were found to be same as that of HOF-SMF case.

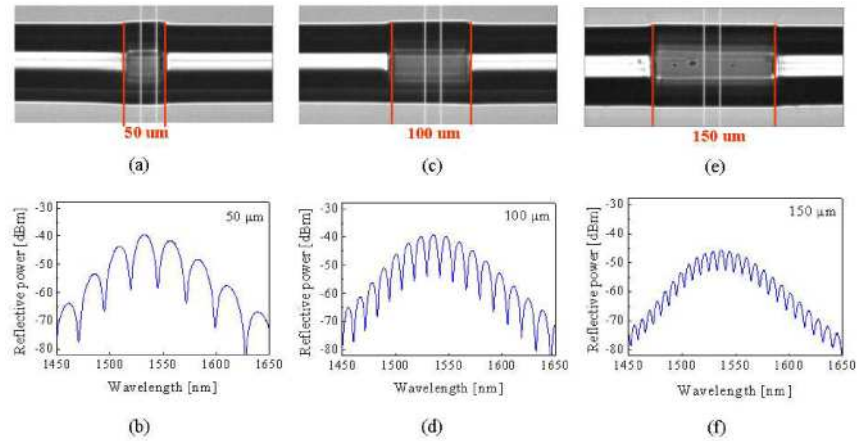


Fig. 3. Microscopic images of HOF cavities and the measured reflection spectra; for the air-gap of (a) 50 μm , (c) 100 μm and (e) 150 μm .

The HOF used in the experiment was in-house fabricated, drawn from a silica tube with a standard optical fiber drawing tower. The inner diameter of the hollow core and the outer diameter of the solid silica cladding of the HOF were 40 μm and 125 μm , respectively, as shown in inset of Fig. 2. Figure 4(a) shows the measured reflection spectrum of the implemented dual-cavity interferometer. The spectrum has two main fringe patterns; a fast varying fringe pattern from the MMF (named as sensing fiber) cavity and a slowly varying one due to the air-cavity. Of course, the overall envelope of the spectrum is governed by the power spectrum of the light source itself. To analyze the behavior of the interference fringes in detail, the spatial frequency spectrum of the interference fringes was calculated by taking FFT and shown in Fig. 4(b). The spatial frequency of the interference spectrum is defined as the number of fringes appeared within a unit spectral width (1 nm for the Fig. 4(b) case).

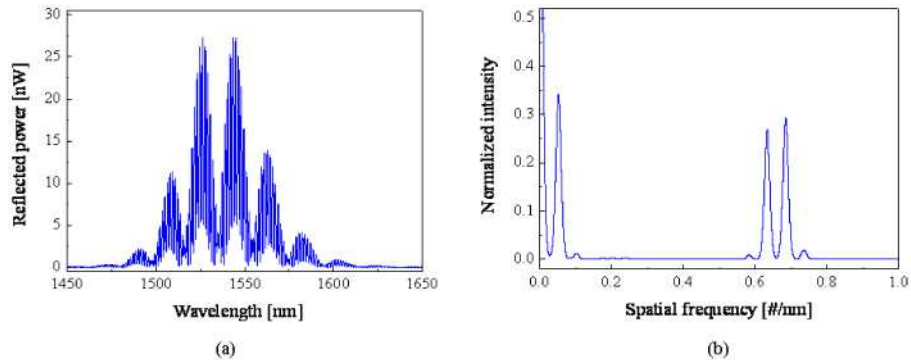


Fig. 4. (a) The reflection spectrum of the fabricated dual-cavity FP interferometer and (b) its spatial frequency spectrum obtained by taking fast Fourier transformation (FFT).

The spatial frequency spectrum as shown in Fig. 4(b) had four dominant frequency components. The DC peak (zero-th peak) and the neighboring first peak correspond to the light source spectrum and the HOF cavity, respectively. The second and third peaks correspond to the only MMF cavity and the composite cavity formed by MMF and HOF, respectively. With this matching, the actual HOF and the MMF lengths were found to be around 71 μm and 503 μm , respectively, which are close to the designed values of 70 μm and

500 μm , respectively. It is noteworthy that there was no appreciable multi-mode effect of MMF due to the short length of HOF.

3. Experimental results and discussion

ERI and temperature measurements are made with the implemented composite-cavity sensor shown in Fig. 2. The ERI measurements were made by dipping the sensor head in standard index liquids (Cargille Laboratories Inc.), which had a quoted accuracy of ± 0.002 . The temperature measurements were performed in a range of 40-500 $^{\circ}\text{C}$ with steps of 20 $^{\circ}\text{C}$.

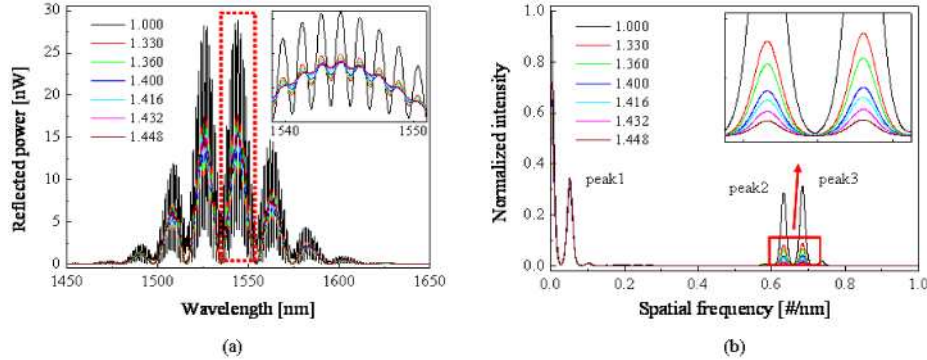


Fig. 5. (a) Reflection spectra of the FP sensor measured with several ERIs. The inset is the close-up of the interference fringes in the dotted red box. (b) Spatial frequency spectra calculated from Fig. 5 (a). The inset is the enlarged one of the red box.

Figure 5 (a) shows the reflection spectra measured with several ERIs in a range of 1.0 to 1.458. As shown in the inset, the fringe contrast was reduced with the ERI increment, which was mainly due to the reduced index difference between the fiber core and the ERI. It should be noted that the reflectivity of the air cavity might not be affected by the ERI change, which can be clearly seen from the spatial frequency spectrum. The spatial frequency spectrum was obtained by taking FFT of the measured spectrum. As shown in Fig. 5(b), the intensities of the second and third peaks were significantly decreased with the ERI increment, while the first peak due to the air cavity did not show any appreciable change. An important feature in the ERI measurement is that there is no shift in the spatial frequency, which is critical in simultaneous measurement of ERI and temperature. Another important feature to be noticed is that the ERI-unaffected peak 1, produced by the HOF cavity, can be used for compensating any undesirable input power fluctuation in principle. In the experiment, we could not see the change of peak 1, which means that the source power or measurement system was quite stable. However, since the light source' power is dependent on the temperature, the compensation process is highly required in harsh environment.

The intensity of the third peak in Fig. 5(b) was plotted in Fig. 6 in terms of ERI. It shows that the sensor response over a wide range of index is well fitted with a quadratic curve but has approximately linear response over the index range from 1.33 to 1.45 as shown in the inset of Fig. 6, which is usually being relevant for biomedical and chemical applications. In the proposed FP interferometer sensor system, the RI measurement is based on the variation of fringe contrast. Since one end of the sensing fiber is protected by the HOF, the ERI response of the sensor is related to the fringe contrast variation caused by changes in the Fresnel reflection at the other end of the sensing fiber exposed to the index specimen.

Because the Fresnel reflection at the air-fiber interface is used to get the interference signal, the reflectance is in the order of a few percent. Further, since the HOF does not act as a waveguide due to the divergence of beam, coupling to the second fiber after passing through HOF is not good in general. However, as already discussed and shown in Fig. 3, for optimum HOF length obtained as 50-100 μm , the interference fringe has a contrast as deep as 10 dB. Therefore, we can say that insertion loss of the HOF will not be a main factor for determining the detection limit of the refractive index. Instead, the instability of the fiber configuration, the

input light source power fluctuation, and the measurement accuracy of the OSA are more dominant. When the system noise is negligible, from the RI sensitivity in the wavelength spectrum, around 16 dB/RIU (Refractive Index Unit), and the amplitude resolution of OSA, 0.001 dB, the RI measurement resolution or detection limit is calculated approximately as 6.2×10^{-5} [26].

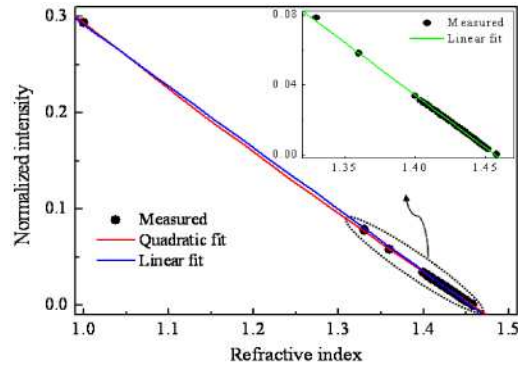


Fig. 6. The magnitude of the peak 3 in Fig. 5 (b) measured and plotted in terms of ERI. It is well fitted with a quadratic curve (red line) rather than with a linear curve (blue line). The inset is the enlarged plot. ERI response can be approximated by linear one over index range 1.33-1.45 (green line)

For the temperature measurement, the proposed sensor was placed in a furnace and the reflection spectrum was measured in a temperature range from 26 °C to 500 °C. Figure 7(a) shows the interference fringe spectra, measured at several temperatures and plotted together. The corresponding spatial frequency spectra are shown in Fig. 7(b).

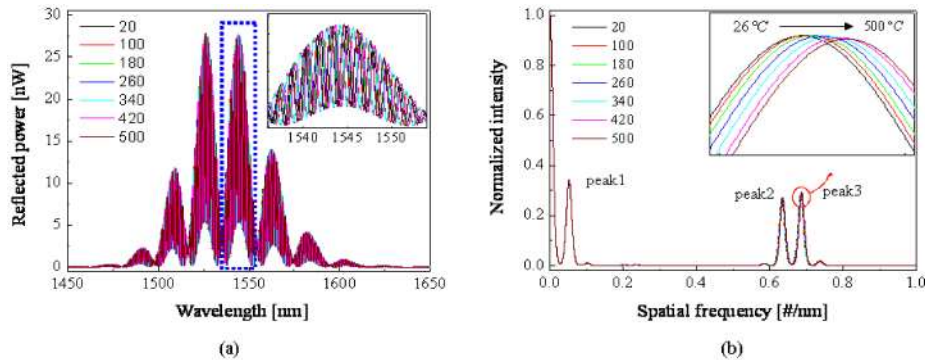


Fig. 7. (a) The reflection spectra measured at several temperatures but plotted together, and (b) the corresponding spatial frequency spectra. The insets are close-up displays.

It can be seen that only the fine interference fringes, due to the MMF cavity, were shifted horizontally without appreciable amplitude variations. On the other hand, the temperature sensitivity of the slowly varying fringes, due to the HOF cavity, was extremely small. This means that the temperature dependency of the HOF cavity was extremely small enough to be neglected in practical applications. The same think can be verified from the first peak of the spatial frequency spectrum. It is also important to note that there is no significant intensity change in the spatial frequency spectrum, which is the critical feature in simultaneous measurement of temperature and ERI. This is in contrast to the ERI measurements, where there is no appreciable shift of the spatial frequency but only intensity variations were observed (see Fig. 5(b)).

Figure 8(a) shows the temperature-induced spatial frequency shift of the peak 3 in Fig. 7(b). The solid line is the fitted curve; the curve fitting was made with a second order

polynomial. The spatial frequency shift was as small as 0.0026/nm with the temperature change of 474 °C (from 26 °C to 500 °C), but big enough to be measured.

For comparison, we replaced the sensor fiber from the MMF to SMF, and the temperature response of SMF sensing cavity was measured as shown in Fig. 8(b). The spatial frequency shift was reduced down to 0.0019/nm for the same temperature span. In addition to this, we have also noticed reduction in the fringe contrast. Comparison between SMF and MMF require further experiments and beyond the scope of this article. However, we believe that the coupling loss due to the smaller core size of SMF is one of the main causes of poor fringe contrast. From the experimental results, we can conclude that MMF acts as a better sensing element than SMF for temperature measurement. And also, the temperature sensitivity can be controlled by the core material of the sensing fiber.

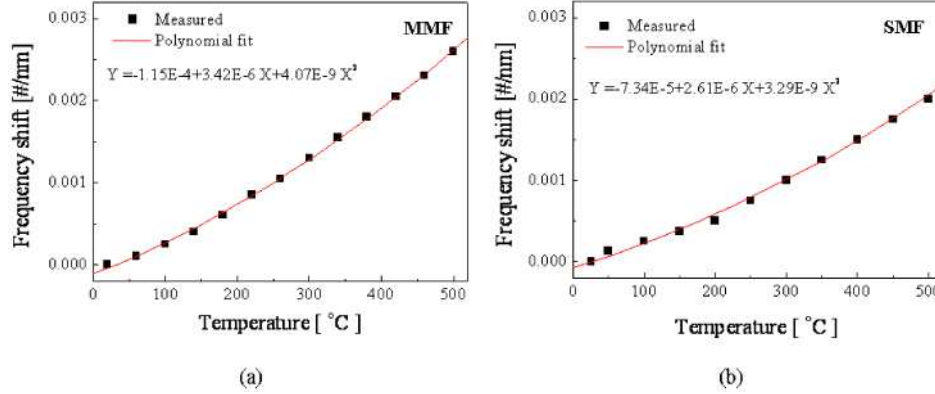


Fig. 8. The temperature responses of MMF cavity (a) and SMF cavity (b). The spatial frequency shifts of MMF and SMF cavity were approximately 0.0026/ nm and 0.0019/nm, respectively, for the temperature change from 26 °C to 500 °C.

From the spatial frequency shift measurements of Fig. 8(a), the change in the round-trip optical path length (OPL) of the MMF cavity, due to temperature variation, can be simply calculated as [27];

$$\Delta l_{OPL} = \lambda_0^2 \Delta \xi \quad (2)$$

Where λ_0 is the center wavelength of the light source and $\Delta \xi$ is the amount of spatial frequency shift due to temperature variation. In the experiment, measured at a center wavelength of 1535 nm, the maximum $\Delta \xi$ was 0.0026/nm with the change of 474 °C (from 26 °C to 500 °C). Therefore, the corresponding temperature-induced round-trip OPL variation, or the optical path length difference (OPD), of the MMF cavity is 6.13 μm .

Considering that the OPL is given by the multiplication between the physical length of the cavity and the refractive index of the cavity waveguide, we can estimate the amount of temperature-induced cavity length variation or the refractive index variation. At first, assuming that temperature change causes only the cavity length variation, the thermal expansion coefficient α of the MMF can be obtained from $\Delta l_{OPL} = n \Delta l = l_{OPL} \alpha \Delta T$ as $8.9 \times 10^{-6} / ^\circ\text{C}$; however, the actual thermal expansion coefficient of fused silica is around 5.5×10^{-7} which is approximately ten times smaller than that of the measured value. Therefore, we need to think of the temperature-induced refractive index variation of the MMF cavity. When we assume only the refractive index variation without thermal expansion, from the relationship of $\Delta l_{OPL} = l \Delta n$, we have the refractive index variation as $\Delta n = 6.13 \times 10^{-3}$, which is reasonable amount. In the above calculation, we have used $n = 1.45$ and $l = 1000 \mu\text{m}$ (double-length of MMF cavity). From this rough calculation performed with the

interference fringe spectrum, even though it is well known, we can say that as a temperature sensor the MMF fiber piece is dominated not by the thermal expansion but by the temperature-induced refractive index variation.

4. Summary and conclusion

In the proposed dual-cavity FP scheme, the principle of simultaneous ERI and temperature measurement can be summarized as follows. The intensity change of the spatial frequency spectrum is caused by only ERI variation, meaning that ERI can be determined solely by monitoring the intensity variation. And also, the shift of the spatial frequency spectrum is originated from only the temperature variation without being affected by ERI. Therefore, the cross-sensitivity problem between temperature and ERI measurements can be solved.

From experimental results, it can be concluded that the proposed dual-cavity FP sensor is suitable for simultaneous measurement of ERI and temperature. The sensor showed an almost linear response to the ERI variation with a resolution (or ERI detection limit) of about 6.2×10^{-5} in the range from 1.33 to 1.45, while the temperature response showed a quadratic behavior with a sensitivity of 8.9-14.6 nm/°C as the temperature was varied in 26-500°C. Since the temperature sensitivity and the ERI resolution of the proposed sensor highly depend on the structure, composition and the fabrication parameters (length of the MMF cavity, doping material of the fiber and splicing conditions), the customizing the sensor can be easily obtained also.

Acknowledgments

This work was supported in part by a grant from the institute of Medical System Engineering (iMSE) in the GIST, Korea and by the Korea Science and Engineering Foundation (KOSEF) grant funded by the Korea government (MEST) (R01-2007-000-20821-0).